Impact and Compensation of Electrical-to-Optical Frequency Response on Carrierless Phase Retrieval Receivers

Qi Gao, Hanzi Huang, Zhengxuan Li, Ziyue Liu, Yuanzhe Qu, and Yingxiong Song

***Abstract*—On carrierless phase retrieval (PR) receivers based on direct detection, bandwidth limitation of electrical-to-optical (E/O) conversion at the transmitter side (Tx) distorts the modulated optical signal. In this paper, we propose the Gercheberg-Saxton (GS)-aided and the data-aided estimation method in order to know the complex-valued of E/O channel response in the absence of phase information. Furthermore, we compare four channel estimation schemes based on the mean square error (MSE) between the estimated and preset channel response in numerical simulation, which are generated by combining least mean square (LMS) or least square (LS) with the proposed GS-aided or data-aided methods. In order to compensate the distortion from E/O frequency response, two compensation schemes including pre-equalization processing at the Tx and post-equalization processing at the Rx are implemented and compared by simulations and experiments. In the experiment, we transmit a single-polarization 30GBaud QPSK signal including a training sequence of 2048 symbols to estimate the E/O conversion frequency response over 55-km single-mode fiber (SMF). The received signal is detected by a PR receiver employing different estimation (LMS/LS) and equalization (pre-/post-) schemes to compare their performance. The experimental results demonstrate that all estimation schemes successfully estimate the frequency response in the absence of phase information, and PR employing pre-equalization with GS-aided-LMS estimation exhibits good robustness, resulting in a received optical power improvement of 0.69 dB to achieve 20% forward-error correction (FEC) threshold.**

***Index Terms*—Coherent optical communications, phase retrieval, equalization.**

I. Introduction

As THE demand for broadband services continues to rapidly escalate, high-capacity optical interfaces are undergoing swift transformations in various domains, including data-center interconnects [1], metro networks [2], and mobile front-haul links [3]. In long-reach scenarios, conventional coherent detection [4] has asserted its dominance by adeptly recovering the entire signal field, effectively mitigating linear impairments like chromatic dispersion (CD), and achieving heightened spectral efficiency through advanced modulation formats. In contrast, cost-effective direct detection [5] approaches dominate short-reach applications such as intra-data center interconnects. Direct detection methods, unlike coherent detection which necessitates interferometric components like a stable local oscillator, a 90-degree optical hybrid, and optical balancing to recover the field information. However, simpler direct detection techniques like on-off keying and PAM4, restricted to accessing solely optical intensity, cannot match the reach and capacity prowess of coherent detection. To bolster the reach and capacity of direct detection systems, advanced direct detection schemes have been proposed, encompassing solutions such as the Kramers-Kronig receiver [6], Stokes-space receiver [7], and transport-of-intensity detection [8]. Despite varying in receiver/transmitter architectures and digital signal processing (DSP) algorithms, those capable of comprehensively measuring the modulated signal field and facilitating equalization necessitate the implementation of a heterodyne detection technique employing a continuous-wave carrier, typically injected at the transmitter prior to signal transmission. Here, it is imperative for the carrier's amplitude to surpass that of the information-bearing signal to meet the minimum phase condition [9] for phase recovery. Consequently, a high carrier-to-signal power ratio (CSPR) emerges, entailing an additional sensitivity penalty. Efforts have been applied to reduce CSPR [10], [11], [12]; however, the carrier is still required.

In recent years, carrierless phase retrieval (PR) receivers have emerged as a simplification to conventional coherent reception structures. These receivers can effectively measure a wide range of complex-valued waveforms pertinent to telecommunications, including Nyquist-shaped Quadrature Amplitude Modulation (QAM) signals, polarization division multiplexing and mode division multiplexing signals [13], [14], obviating the reliance on optical carriers. These carrierless PR receivers demonstrate the feasibility of complete field recovery by utilizing photodiodes (PDs) to capture intensity measurements under varying linear [13] or random [15] projections. Optimization of phases satisfying the projection relationships is subsequently performed.

Manuscript received 2 February 2024; revised 21 February 2024; accepted 25 February 2024. Date of publication 29 February 2024; date of current version 21 March 2024. This work was supported in part by the National Key Research and Development Program of China under Grant 2021YFB2900801, in part by the Science and Technology Commission of Shanghai Municipality under Grant 22511100902, Grant 22511100502, Grant 20511102400, and Grant 20ZR1420900, and in part by 111 Project under Grant D20031. *(Corresponding author: Yingxiong Song.)*

The authors are with the Key Laboratory of Specialty Fiber Optics and Optical Access Networks, Shanghai University, Shanghai 200444, China (e-mail: gaoqi21225136@shu.edu.cn; hanzihuang@shu.edu.cn; zhengxuanli@shu.edu.cn; lzyPG85@shu.edu.cn; quyuanzhe@shu.edu.cn; herosf@shu.edu.cn).

Digital Object Identifier 10.1109/JPHOT.2024.3371500

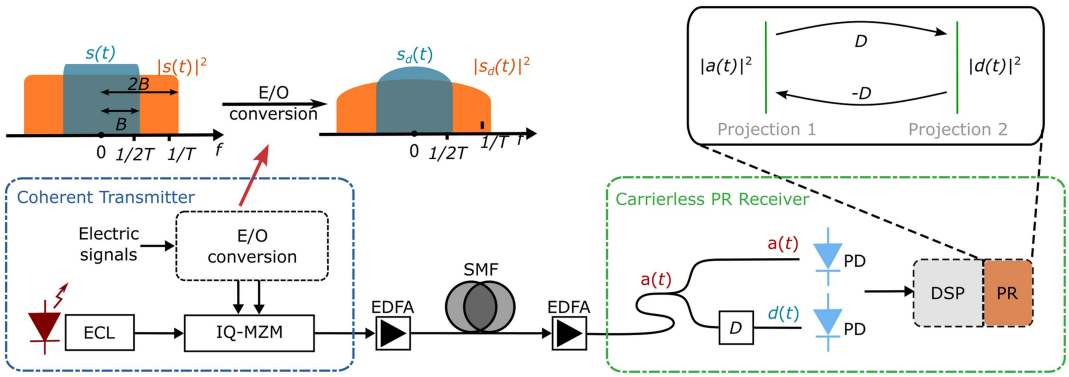

Fig. 1. Optical transmission system and carrierless PR receiver based on direct detection.

A single complementary linear projection, harnessed through a modified Gerchberg-Saxton (GS) algorithm with selective phase reset and pilot symbols [13], proves sufficient for phase retrieval in complex-valued signal scenarios. More projections generally can provide better convergence [15], [16] at the expense of increased hardware complexity. However, the electrical-to-optical (E/O) conversion at the transmitter introduces distorted modulated optical signal. These distortion can happen in the complex-value domain and needs optical phase measurement to estimate its corresponded channel response, which cannot be afforded by intensity-only detection. Taking advantage of the fact that the phase of the training sequence is known, the response of the complex-valued channel can be estimated only through the intensity information, thereby realizing the complex channel estimation of the PR receiver. Regarding the study of equalization of nonlinear impairments of PR systems in higher-order modulation formats, we have proposed solutions and verified them experimentally [17].

In this paper, we explore the impact of E/O frequency response and its compensation techniques on carrierless PR receivers. We propose two methods, GS-aided and data-aided, in the absence of signal phase information, and based on these, four channel estimation schemes and two equalization structures are given. In order to study their performance rules under different frequency response bandwidth limitations and optical signal-to-noise ratios (OSNRs), we compare these estimation schemes through numerical simulations. In simulation, we also explore the feasibility of improving PR recovery accuracy through pre-equalization/post-equalization after channel estimation, and find that pre-equalization is more robust than post-equalization. In order to further verify the simulation results, we build an experimental platform and compare different schemes by transmitting a single-polarization carrierless 30-GBaud QPSK signal with a roll-off factor $\beta = 0.01$. Experimental results show that, among the four schemes, the optimal performance is achieved by the pre-equalization scheme based on GS-aided-LMS method, which improves the received optical power (ROP) sensitivity by 0.69 dB, and reduces the bit-error rate (BER) after complete convergence from 6.9×10^{-3} to 2.2×10^{-3}.

II. Principle of the E/O Frequency Response Estimation

A. Impact of E/O Frequency Response on PR Receivers

Fig. 1 delineates the optical transmission system employing PR field reconstruction, encompassing the coherent transmitter and the carrierless PR receiver based on direct detection. The coherent transmitter comprises an External Cavity Laser (ECL), and an IQ-Mach-Zehnder modulator (MZM). The modulated optical signal, following amplification through the Erbium-Doped Fiber Amplifier (EDFA), traverses the single-mode fiber (SMF) link and subsequently interfaces with the carrierless PR receiver. The carrierless PR receiver is composed of a splitter, a dispersive element with a dispersion coefficient D, and two photodetectors (PDs). $a(t)$ is the complex-valued optical field after transmission and $d(t)$ is the complex-valued optical field after transmitting over the dispersive element with chromatic dispersion value of D. $|a(t)|^2$ and $|d(t)|^2$ are intensity measurements. Typical PR receivers employ a GS iteration scheme with the aid of selective phase reset and pilot constraint to search for optimum phases. In the context of complex-valued signals like QPSK, a solitary complementary linear projection serves as a satisfactory method to recover the phase. After direct detection, the bandwidth $|s(t)|^2$ enlarges to $2B$, where B represents the bandwidth of the transmitted complex-valued optical signal, and T signifies the symbol rate. The transmitted complex optical field is distorted causing by the transmitter as

$$s_d(t) = s(t) * h_{tx}(t), \tag{1}$$

where $h_{tx}(t)$ denotes the impulse response induced by the E/O time response at the transmitter. $*$ denotes the convolution operator. Given the loss of phase information in $h_{tx}(t)$ resulting from the direct detection procedure, the straightforward equalization of optical intensity cannot effectively rectify $h_{tx}(t)$, which is different from the distortion caused by Optical-to-Electrical (O/E) frequency response for carrierless PR receivers [18]. Therefore, it is necessary to design algorithms specialized in complex-valued channel estimation in the absence of phase information and equalization schemes to compensate the distortion from E/O frequency response.

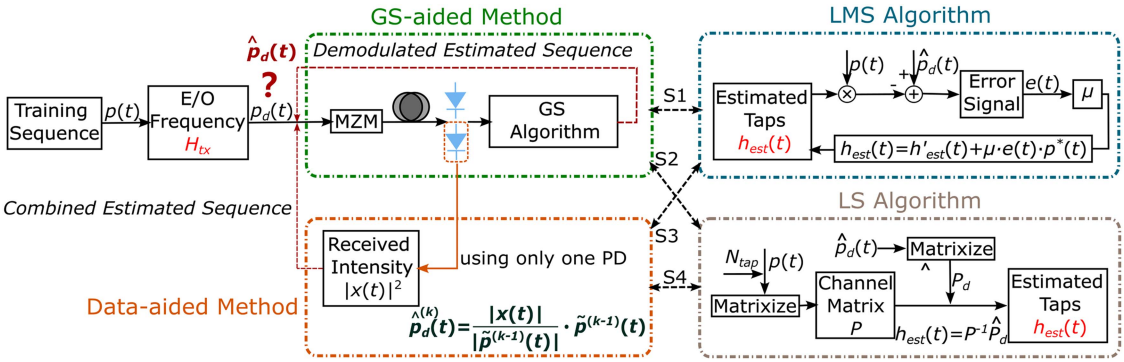

Fig. 2. Schematic diagrams of the four estimation schemes including the structure of GS-aided method, data-aided method, LMS algorithm, and LS algorithm.

B. E/O Frequency Response Estimation Schemes

For the purpose of estimating the distortion pattern introduced by the transmitter channel when phase information is unavailable, a training sequence denoted as $p(t)$ is transmitted, encompassing 2048 training QPSK symbols. It is presumed that these symbols are pre-known to the receiver. The initial step entails the recovery of the complete field of the distorted signal attributed to the E/O frequency response. To this end, two estimation methods, namely the Gerchberg-Saxton (GS)-aided method and the data-aided method, have been proposed. These methods get the estimation of the impulse response denoted as $h_{tx}(t)$ from the distorted training sequence $p_d(t)$ as

$$p_d(t) = p(t) * h_{tx}(t), \tag{2}$$

where the GS-aided method uses alternative projection between two measured intensity waveforms and the data-aided method combines one measured amplitude waveform with the phase of $p(t)$. After successfully estimating the distorted training sequence $p_d(t)$, the impulse response associated with the E/O conversion can be calculated. This process is enabled through the utilization of both the unaltered training sequence $p(t)$ and the inferred estimation $p_d(t)$, employing either the least mean square (LMS) algorithm or the least mean square (LS) algorithm. Both the LMS algorithm [19] and the LS algorithm [20] are integrated with the proposed estimation method, resulting in the formulation of four distinct estimation schemes: GS-aided-LMS ($S1$), GS-aided-LS ($S2$), data-aided-LMS ($S3$), and data-aided-LS ($S4$). Fig. 2 shows the schematic diagrams of the four estimation schemes.

1) $S1$ & $S2$: As depicted in Fig. 2, the core essence of the GS-aided estimation methodology revolves around the utilization of the Gerchberg-Saxton (GS) algorithm. This algorithm is harnessed to facilitate the estimation of the distorted training sequence denoted as $p_d(t)$. Subsequently, the LMS algorithm or LS algorithm is employed to deduce the Electrical-to-Optical (E/O) frequency response. After fiber channel transmission, two independent intensity waveforms corresponding to varying dispersion levels of the distorted training sequence $p_d(t)$ are detected by PDs. In conventional GS algorithm [13], the estimated complex field encompasses amplitude information derived from measured intensity, combined with a sequence of random phases serving as the initial approximation. To ensure full convergence performance, the iteration count is usually set at more than one hundred. However, given the premise of knowledge about the training sequence at the Rx, the modified GS algorithm can employ $p(t)$ as the initial approximation to obtain the estimation of $p_d(t)$, denoted as $\hat{p}_d(t)$. Algorithm 1 provides the pseudocode of the GS-aided method. For the sake of simplicity, we write the pseudocode in the time domain. Both GS-aided method and data-aided method are implemented in the frequency domain using fast Fourier transform (FFT) and its inverse (IFFT). The amplitude information $|a_p(t)|$ and $|b_p(t)|$ is computed from the intensity measurements of the training signals of both branches. $*$ is the convolution operator. $h_{CD}(t)$, $h_D(t)$, $h_{BW}(t)$ are, respectively, the impulse responses of the transmission fiber, the dispersive element for alternative projection, and a brick-wall low-pass filter as a signal spectral constraint, whose passband is B. The computational complexity of the GS-aided method for each processing block can be estimated as $\mathcal{O}(NFT\log_2 T)$, where N, F, T represent the number of iterations required inside the GS-aided algorithm, the FFT/IFFT operations per iteration, and the block size.

In scheme $S1$, subsequent to the estimation of $\hat{p}_d(t)$ through the utilization of the GS-aided method, the estimated impulse response $h_{est}(t)$ are iteratively updated until convergence is achieved facilitated by the adoption of LMS algorithm as

$$h_{est}(t) = h'_{est}(t) + \mu \cdot e(t) \cdot p^*(t) \tag{3}$$

and

$$e(t) = \hat{p}_d(t) - p(t) \cdot h_{est}(t), \tag{4}$$

where $e(t)$ signifies the error signal which functions as a metric for gauging the convergence status of the LMS algorithm; $h'_{est}(t)$ represents the tap estimated by the previous iteration and is initialized to all zeros with the number of taps N_{tap}; μ is the step size and set to 1.0×10^{-3}; $p^*(t)$ corresponds to the conjugate of $p(t)$. Similarly, we show the pseudo-code flow of data-aid in Algorithm 2. For $S2$, the approach differs as LS algorithm is chosen over LMS algorithm used in $S1$ to derive the estimated impulse response $h_{est}(t)$. The channel matrix P [21] is constructed according to the number of taps N_{tap} and the length of the digitized training sequence $p(t)$ which is denoted as L. The matrix P has a dimensionality characterized by the

Algorithm 1: Distorted Training Sequence Estimator Based on GS-aided Method.

$\hat{p}_d(t) \leftarrow p(t)$ ▷ Initial approximation
$\hat{p}_d(t) \leftarrow h_{CD}^{-1}(t) * \hat{p}_d(t)$ ▷ To transmitter
for i in N **do**
  $\hat{p}_d(t) \leftarrow h_D(t) * h_{CD}(t) * \hat{p}_d(t)$ ▷ To projection 2
  $\hat{p}_d(t) \leftarrow |d_p(t)| \exp j\angle\hat{p}_d(t)$ ▷ Amplitude constraint
  $\hat{p}_d(t) \leftarrow h_D^{-1}(t) * \hat{p}_d(t)$ ▷ To projection 1
  $\hat{p}_{d,pre}(t) \leftarrow h_{CD}^{-1}(t) * \hat{p}_d(t)$ ▷ A copy to transmitter
  $\hat{p}_d(t) \leftarrow |a_p(t)| \exp j\angle\hat{p}_d(t)$ ▷ Amplitude constraint
  $\hat{p}_d(t) \leftarrow h_{CD}^{-1}(t) * \hat{p}_d$ ▷ To transmitter
  $Err_{GS}(t) \leftarrow ||\hat{p}_{d,pre}(t)| - |\hat{p}_d(t)||^2$ ▷ Calculate Error
  $\hat{p}_d(t) \leftarrow h_{BW}(t) * \hat{p_d}(t)$ ▷ Spectrum constraint
  $\hat{p}_d(t) \leftarrow \hat{p}_d(t) * \sqrt{\mathbb{E}(|\hat{p}_d(t)|^2)}$ ▷ Power normalization
end for
return $\hat{p}_d(t)$

number of rows, which corresponds to N_{tap}, and the number of columns, which aligns with L. P is constructed as below

$$P = \begin{bmatrix} p(0) & p(1) & \dots & p(L-1) \\ p(-1) & p(0) & \dots & p(L-2) \\ \vdots & \vdots & \ddots & \vdots \\ p(1-N_{tap}) & p(2-N_{tap}) & \dots & p(L-N_{tap}) \end{bmatrix}_{N_{tap}\times L}, \tag{5}$$

Correspondingly, the estimated distorted training sequence $\hat{p}_d(t)$ is digitized and transformed into column matrix form as $\hat{P}_d$. Then the computation of the estimated impulse response $h_{est}(t)$ is conducted through the following as

$$h_{est}(t) = P^{-1}\hat{P}_d, \tag{6}$$

where P^{-1} represents the pseudo-inverse of matrix P.

The LMS algorithm considers the impact of noise while the LS estimation algorithm ignores it. Therefore, the estimation error of the LS estimation algorithm will be larger under low OSNRs [19], [20]. Regardless of $S1$ or $S2$, the GS-aided method is utilized to perform the iterative training sequence $p(t)$ of the dual optical field to estimate the distorted training sequence.

2) $S3$ & $S4$: Rather than employing two intensity waveforms for the purpose of dual-field iterations, the data-aided method acquires $\hat{p}_d(t)$ by iteratively combining the amplitude information $x(t)$ from a given received waveform with the phase of $\tilde{p}^{(k)}(t)$. Here, the superscript $^{(k)}$ denotes the iteration index, and $\tilde{p}^{(k)}(t)$ results from

$$\tilde{p}^{(k)}(t) = \tilde{p}^{(k-1)}(t) * h_{est}^{(k-1)}(t), \tag{7}$$

where $\hat{p}_d^{(k)}(t)$ is updated by

$$\hat{p}_d^{(k)}(t) = \frac{|x(t)|}{|\tilde{p}^{(k-1)}(t)|} \cdot \tilde{p}^{(k-1)}(t) \quad (k = 1, 2, \dots, M). \tag{8}$$

The initial value of $\tilde{p}^{(k)}(t)$ is established as $\tilde{p}^{(0)}(t) = p(t)$, and the evolution of $h_{est}^{(k)}(t)$ is updated through the utilization of either the LMS algorithm or the LS algorithm, thereby categorizing the process into $S3$ and $S4$. M is the total number of iterations of the data-aided method, which only requires a single PD. In this paper, $M = 7$. Similarly, we show the pseudo-code flow of data-aid method in Algorithm 2. The computational complexity of the data-aided method is lower than that of the GS-aided method, which is $\mathcal{O}(MF)$. M is the number of iterations of the data-aided algorithm and F represents the FFT/IFFT operations per iteration. In $S3$, $h_{est}^{(k)}(t)$ is updated using LMS as

$$h_{est}^{(k)}(t) = h_{est}^{\prime(k)}(t) + \mu^{(k)} \cdot e^{(k)}(t) \cdot \tilde{p}^{(k)*}(t), \tag{9}$$

and

$$e^{(k)}(t) = \hat{p}_d^{(k)}(t) - \tilde{p}^{(k)}(t) \cdot h_{est}^{(k-1)}(t) \quad (k = 1, 2, \dots, M), \tag{10}$$

where the optimal value of the parameter $\mu^{(k)}$ is set at a constant value of 1.3×10^{-3}. In the framework of $S3$, each iteration of the data-aided method entails the complete execution of the LMS algorithm. On the other hand, in $S4$ which employs the LS algorithm, the estimated E/O impulse response of each iteration is updated by

$$h_{est}^{(k)}(t) = \tilde{P}^{(k)-1}\hat{P}_d^{(k)} \quad (k = 1, 2, \dots, M). \tag{11}$$

Here, the matrix $\tilde{P}^{(k)}$ signifies the matrix derived from $\hat{p}_d^{(k)}(t)$ and has a dimensionality characterized by the number of rows N_{tap} and the number of columns is L. $\tilde{P}^{(k)-1}$ denotes the pseudo-inverse of $\tilde{P}^{(k)}$, and $\hat{P}^{(k)}d$ is the column matrix formed from $\hat{p}^{(k)}d(t)$ values. Ultimately, whether in the context of $S3$ or $S4$, each iteration's estimated impulse response $h_{est}^{(k)}(t)$ is concatenated to construct the complete estimated channel $h_{est}(t)$ as follows:

$$h_{est}(t) = h_{est}^{(1)}(t) * h_{est}^{(2)}(t) * \dots * h_{est}^{(k)}(t)(k = 1, 2, \dots, M), \tag{12}$$

Subsequently, the equalization impulse response $h_{eq}(t)$ is deduced by computing the inverse of $h_{est}(t)$.

We now consider the computational complexity of the four estimation algorithms. Since the four estimation algorithms are a combination of the GS-aided and data-aided methods with the LMS and LS algorithms, and the computational complexity of the GS-aided and data-aided methods has been given earlier, the complexity of the LMS and LS algorithms also needs to be considered. For the LMS algorithm, the computational complexity is $\mathcal{O}(N_{tap}T\log_2 T)$. On the other hand, the computational complexity of the LS algorithm is $\mathcal{O}(N_{tap}L)$. Therefore, the computational complexity of $S1$, $S2$, $S3$, and $S4$ are $\mathcal{O}[(NF + N_{tap})T\log_2 T]$, $\mathcal{O}[NFT\log_2 T + N_{tap}L]$, $\mathcal{O}(MFN_{tap}T\log_2 T)$, and $\mathcal{O}(MFN_{tap}L)$, respectively.

Algorithm 2: E/O Response Estimator Based on Data-aided Method.

$\tilde{p}^{(0)}(t) \leftarrow p(t)$ ▷ Initial value
$h_{est}^{(0)}(t) \leftarrow \delta(t)$ ▷ Initial guess of E/O response
for $k = 1, 2, \ldots, M$ **do**
  $\tilde{p}^{(k)}(t) \leftarrow \tilde{p}^{(k-1)} * h_{est}^{(k-1)}(t)$ ▷ Calculate distorted signal
  $\hat{p}_d^{(k)}(t) \leftarrow |x(t)| \exp j\angle\tilde{p}^{(k-1)}(t)$ ▷ Combine amplitude
    if $S3$ **then**
      Calculate $h_{est}^{(k)}(t)$ with LMS channel estimation
    else if $S4$ **then**
      Calculate $h_{est}^{(k)}(t)$ with LS channel estimation
  end if
end for
return $\hat{p}_d^{(k)}(t), h_{est}^{(k)}(t)$

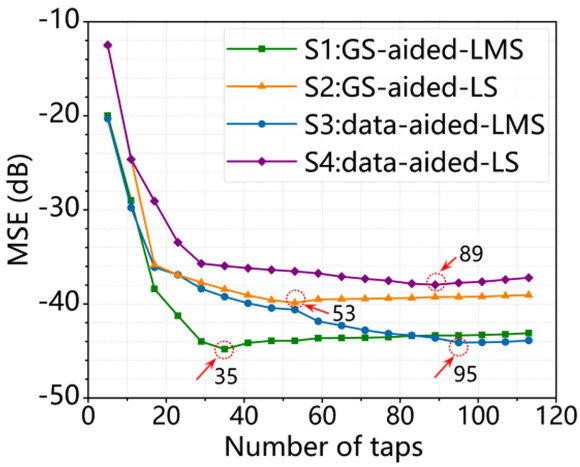

Fig. 3. Simulated MSEs for the schemes versus the number of taps at OSNR = 30 dB.

C. Simulated Performance of the Estimation Schemes

We simulate a setup for detecting a 30-Gbaud Nyquist-shaped QPSK signal with a roll-off factor $\beta = 0.01$ after 55-km SMF transmission using a carrierless PR receiver. We employ the ideal rectangular low pass filter to simulate E/O bandwidth, which is denoted as H_{tx} and set at 13.5 GHz. We first investigate the performance of the estimation schemes versus the number of taps at OSNR = 30 dB and bandwidth = 13.5 GHz as is shown in Fig. 3. We find that MSE decreases to a minimum value as the number of taps increases. The optimal number of taps for $S1$, $S2$, $S3$, and $S4$ under optimal MSE performance are respectively 35, 53, 95, and 89. Data-aided based $S3$ and $S4$ employ single intensity signal to estimate E/O response, contributing to the larger number of required taps than GS-adied based $S1$ and $S2$ to obtain higher estimation accuracy. Consequently, $S3$ and $S4$ have better MSE performance at larger taps.

The same training sequence $p(t)$ is applied in each scheme. We have tried different lengths of training sequences, including 2048, 20480, and 204800 symbols, and find no significant changes in performance. Therefore we choose 2048 for training length. To match the parameters used in the experiment, CD from 55-km SMF transmission and alternative projection with the dispersion of 505 ps/nm are used.

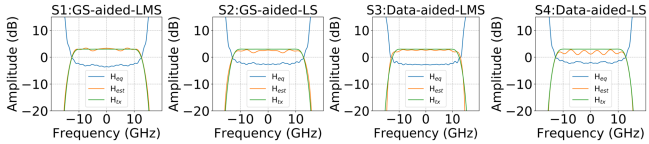

Fig. 4. Curves of H_{tx}, H_{est}, and H_{eq} denoted as the preset frequency response in simulation, estimated frequency response and equalizer frequency response.

The Fourier transforms of $h_{est}(t)$ and $h_{eq}(t)$ are denoted as H_{est} and H_{eq}, respectively. Curves of H_{tx}, H_{est}, and H_{eq} under the four estimation schemes are shown in Fig. 4. Observing the plots, it becomes apparent that the H_{est} of all schemes to some extent approximate the preset E/O frequency response.

We speculate that the performance of all estimation schemes is interconnected with the preset bandwidth limitation of E/O frequency response and the OSNR of the transmission link. Therefore, we investigate the performance of the four estimation schemes in simulation under different E/O bandwidth limitations and OSNR conditions (assuming that the frequency response bandwidth of the I-channel and the Q-channel are identical), where the mean square error (MSE) between the estimated impulse response and the preset impulse response is adopted as the performance indicator for evaluating the estimation scheme as shown in Fig. 5(a). As the OSNR of the link increases, the MSE associated with the four estimation schemes progressively diminishes. This observation affirms the notion that the OSNR of the link constitutes one of the key factors influencing the performance of E/O frequency response estimation. The challenge associated with the estimation of dual optical field channels lies in the accumulation of magnitude errors within the measurements, consequently impacting the overall estimation efficacy. In addition, it can be found that with the increase of E/O bandwidth, the MSE of $S1$ and $S3$ decreases more significantly than that of $S2$ and $S4$. Fig. 5(b) shows MSEs for the four schemes versus OSNRs at E/O bandwidth limitations = 12, 13, and 14 GHz, respectively. When the E/O bandwidth is 14 GHz, the MSEs corresponding to the ONSR increase from 12 dB to 30 dB under $S1$ and $S3$ decreases by 7.37 dB and 7.12 dB, respectively, while the MSE under $S2$ and $S3$ decreases by 4.65 dB and 3.48 dB, respectively. Fig. 5(c) shows MSEs for the four schemes versus E/O bandwidth limitations at OSNR = 18, 24, and 30 dB. As the predetermined E/O frequency response bandwidth is expanded, a corresponding downward trend is observed in the Mean Square Error (MSE) of all four schemes. This behavior can be attributed to the fact that with a wider E/O frequency response bandwidth, the estimation of the distorted training sequence becomes more accurate, consequently enhancing the overall estimation performance. This observation validates the notion that the limitation imposed by the E/O frequency response bandwidth is indeed a crucial factor influencing the estimation performance of the four schemes. A longitudinal analysis reveals that MSE of schemes $S1$ and $S3$, utilizing the LMS algorithm,

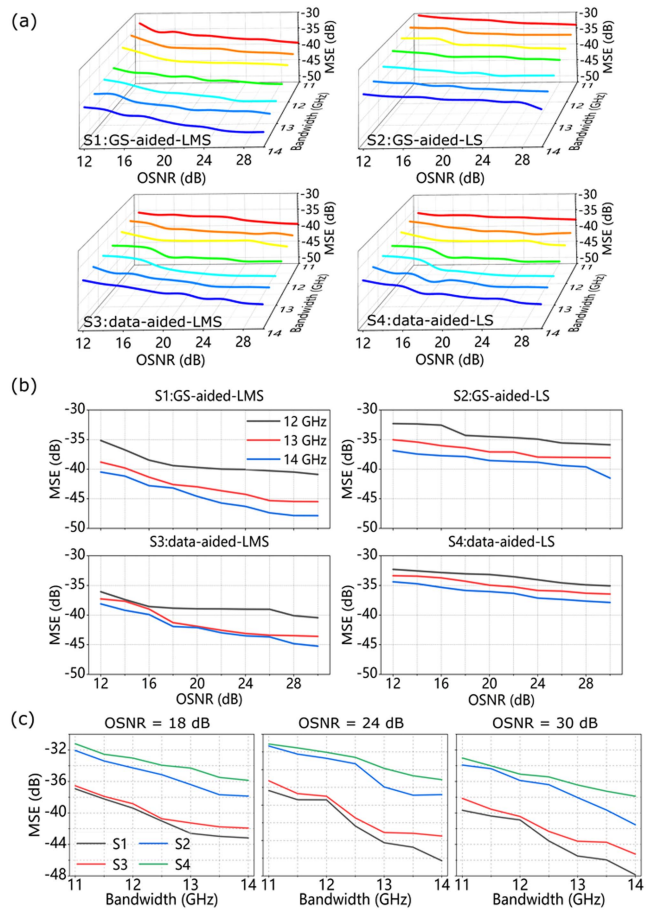

Fig. 5. Simulated (a) MSEs for the four schemes versus OSNRs and E/O bandwidth limitations, (b) MSEs for the four schemes versus OSNRs, (c) MSEs for the four schemes versus E/O bandwidth limitations at OSNR = 18, 24, and 30 dB.

is notably lower than that of schemes $S2$ and $S4$, employing the LS algorithm.

III. Principle of the E/O Frequency Response Compensation

A. E/O Frequency Response Compensation Schemes

Upon successfully estimating the E/O conversion's frequency response, the subsequent stage of our research is to design E/O frequency response compensation schemes based on the result of four estimation schemes. We present pre-equalization and post-equalization compensation schemes, positioned respectively at the Tx and the Rx of the transmission system.

1) Pre-Equalization: Schematic of pre-equalization is shown in Fig. 6. The fundamental principle of pre-equalization involves subjecting the electrical signal to be transmitted to pre-processing through a finite impulse response equalizer [22]. As the frequency response H_{eq} of the pre-equalizer corresponds to the inverse of H_{est} obtained from the four estimation schemes, theoretically the frequency response of the cascaded pre-equalizer and E/O conversion H_{tx} tends to approach a constant value. Indeed, the efficacy of pre-equalization

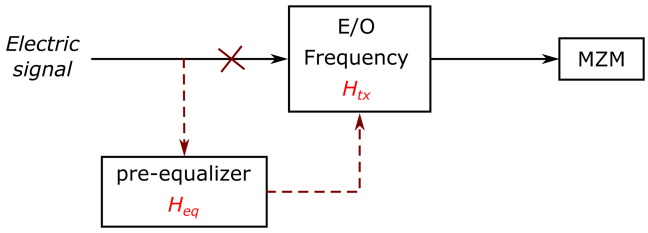

Fig. 6. Schematic of pre-equalization at the transmitter side.

is intricately tied to the estimation performance of each estimation scheme. Attaining accurate estimation of the E/O frequency response H_{eq} can significantly enhance the efficacy of pre-equalization. The pre-equalization scheme offers the advantage of equalizing the electrical signal prior to its entry into the optical modulator, ensuring promptness in the process. However, the drawback lies in the potential escalation of system complexity at the Tx.

To verify the spectrum recovery achieved by pre-equalization on electric signals distorted by E/O frequency response, we conducted simulations to obtain estimation outcomes for the four proposed estimation schemes. The preset E/O conversion bandwidth limitations both for the I-channel and the Q-channel are set at 13.5 GHz. All four estimation schemes are conducted at 30 dB OSNR. Fig. 7 shows the spectrum comparison of electric signals before and after pre-equalization. Prior to the implementation of pre-equalization, the spectrum of the transmitted electrical signal exhibits significant distortion following the E/O conversion, as compared to the original field. However, with the introduction of pre-equalization, the spectrum of the distorted electrical signal is effectively recovered across all four estimation schemes.

2) Post-Equalization: Algorithm 3 shows the detailed pseudocode for the post-equalization scheme. In the post-equalization scheme, the compensation module is integrated with the GS algorithm at the Rx. Within the GS algorithm, complex-valued signals are estimated by amplitude constraint between the transmitter and two projections iteratively until the error stops decreasing. H_{est} and H_{eq} are introduced before and after pilot constraint at the transmitter plane. The purpose is to simulate the distortion process of the complex field signal caused by H_{tx} during the iterative process, so as to estimate the original electrical signal more accurately Fig. 8. The post-equalization scheme's advantage lies in its ability to achieve E/O frequency response compensation solely through the enhanced GS algorithm. However, since the improved GS algorithm iterate the light field between different projections, the error between the estimated H_{est} and the actual H_{tx} will be accumulated, affecting the convergence ability of the GS algorithm and the performance of phase retrieval. For the sake of simplicity, we write the pseudocode in the time domain. Both pre-equalization and post-equalization are implemented in the frequency domain using FFT and IFFT. Within each iteration, the estimated field $\hat{s}(t)$, dual complex field $a(t)$ and $b(t)$ are operated at two samples per symbol (SPS). At the start of the GS algorithm, amplitude information $|a(t)|$ and $|b(t)|$ is calculated

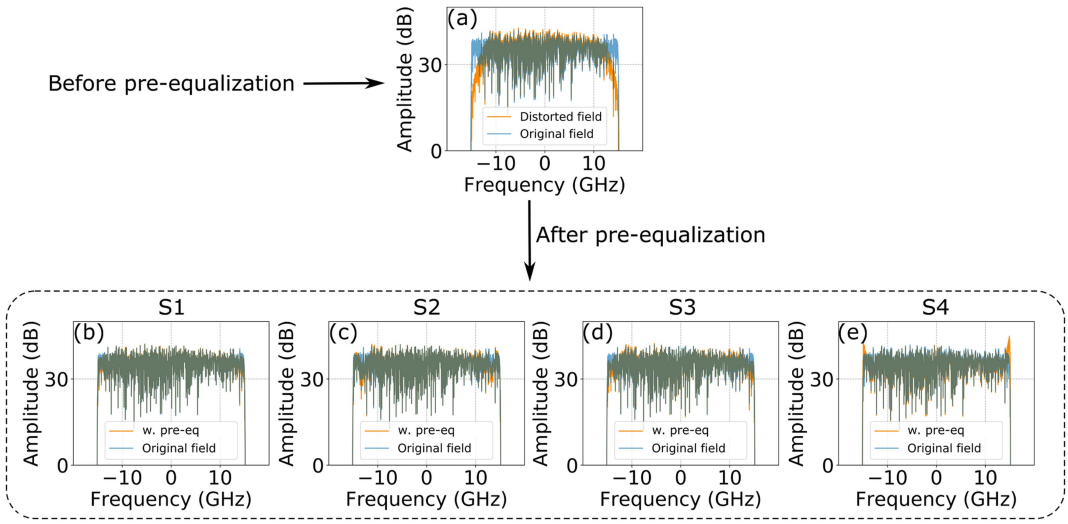

Fig. 7. (a) Spectrum comparison between the original field and the distorted field before pre-equalization; Spectrum comparison between the original field and the recovered field after pre-equalization under (b) $S1$, (c) $S2$, (d) $S3$, (e) $S4$, respectively.

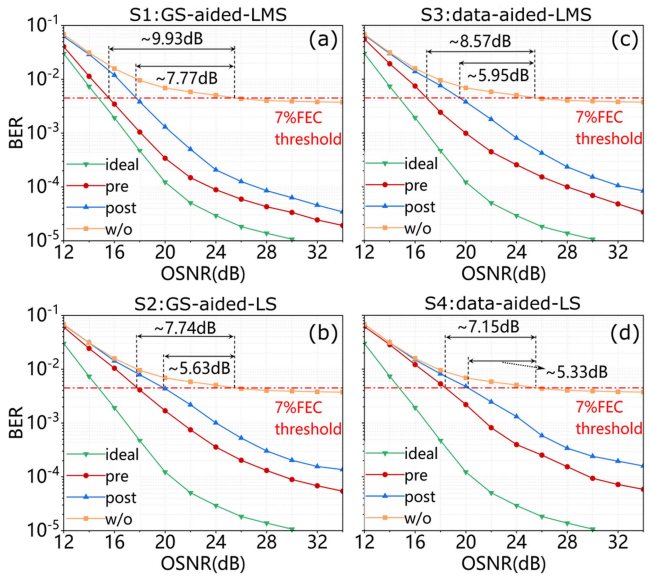

Fig. 8. Simulated BERs versus OSNRs (I-channel = 13.5 GHz and Q-channel = 13 GHz) under (a) $S1$, (b) $S2$, (c) $S3$, (d) $S4$.

over the measured intensity by square root operation. $h_{est}(t)$, $h_{eq}(t)$ are, respectively, the estimated impulse response and equalization impulse response of E/O conversion. At the phase reset process, $rand(t)$ obeys standard normal distribution. The post-equalization scheme for each processing block provides the same complexity order of $\mathcal{O}(NFT\log_2 T)$ with the GS-aided method.

B. Simulated Performance of the Pre-Equalization and Post-Equalization

We carry out simulations consistent with the simulation in Section II-C to characterize the performance of the pre-equalization and post-equalization. The modified GS algorithm is operated in a block-wise manner with with a 20% pilot symbol ratio. The interval for phase reset, K, is set to 5. A is set to 20 at two SPS of $\hat{s}(t)$ to make a 10-symbol-wide moving average for both cases. One hundred blocks with different noise realizations are used to calculate the BER. We studied the impact of two factors including OSNR and E/O bandwidth limitation on the performance of pre-equalization and post-equalization respectively.

We compare the influence of OSNR on the performance of pre-equalization and post-equalization based on different estimation schemes. We preset here that the bandwidths of the I channel and the Q channel are not identical to simulate the general situation in the experiment. It is worthwhile to note that the small difference in the bandwidths of the two channels hardly affects the estimated performance of the four scenarios. Fig. 8 shows the BERs versus OSNRs (I-channel = 13.5 GHz and Q-channel = 13 GHz) to achieve a 7% forward-error correction (FEC) threshold at BER of 4.5×10^{-3} under four estimation schemes. In contrast to the absence of compensation schemes, both pre-equalization and post-equalization substantially enhance the demodulation performance of the system. In the case of pre-equalization schemes based on $S1$, $S2$, $S3$, and $S4$, respectively, the OSNR sensitivity has increased by 9.93, 8.57, 7.74, and 7.15 dB. In the corresponding post-equalization case, the OSNR sensitivity has increased by 7.77, 5.95, 5.63, and 5.33 dB, respectively. The simulation results demonstrate that pre-equalization based on the four estimation schemes outperforms post-equalization. This is due to the fact that pre-equalization compensates for impairments before intensity-only detection, resulting in less accumulated error in GS iterations than post-equalization. The essence of pre-equalization is to pre-process the transmitted signal at the transmitter side to compensate for signal distortion caused by the E/O response. The signal distortion is significantly reduced after pre-equalization, thus attenuating the noise that enters inside the GS algorithm at the receiver side and avoiding the increase of the algorithm

Algorithm 3: Modified PR Algorithm with Post-equalization.

$\hat{s}(t) \leftarrow |a(t)| \exp j\angle rand(t)$ ▷ Initialize phase
$\hat{s}(t) \leftarrow h_{CD}^{-1}(t) * \hat{s}(t)$ ▷ To transmitter
for i in N **do**
  $\hat{s}(t_p) \leftarrow |\hat{s}(t_p)| \exp j\angle s(t_p)$ ▷ Pilot constraint
  $\hat{s}(t) \leftarrow h_{est}(t) * \hat{s}(t)$ ▷ Estimated E/O impulse response
  $\hat{s}(t) \leftarrow h_D(t) * h_{CD}(t) * \hat{s}(t)$ ▷ To projection 2
  $\hat{s}(t) \leftarrow |d(t)| \exp j\angle \hat{s}(t)$ ▷ Amplitude constraint
  $\hat{s}(t) \leftarrow h_D^{-1}(t) * \hat{s}(t)$ ▷ To projection 1
  $\hat{s}_{pre}(t) \leftarrow h_{CD}^{-1}(t) * \hat{s}(t)$ ▷ A copy to transmitter
  $\hat{s}(t) \leftarrow |a(t)| \exp j\angle \hat{s}(t)$ ▷ Amplitude constraint
  $\hat{s}(t) \leftarrow h_{CD}^{-1}(t) * \hat{s}(t)$ ▷ To transmitter
  $Err_{GS}(t) \leftarrow ||\hat{s}_{pre}(t)| - |\hat{s}(t)||^2$ ▷ Calculate Error
  $\hat{s}(t) \leftarrow h_{eq}(t) * \hat{s}(t)$ ▷ Equalize
  $\hat{s}(t) \leftarrow h_{BW}(t) * \hat{s}(t)$ ▷ Spectrum constraint
  $\hat{s}(t) \leftarrow \hat{s}(t) * \sqrt{\mathbb{E}(|\hat{s}(t)(t)|^2)}$ ▷ Power normalization
  if $i \bmod K = 0$ **then**
    $Err_{GS}^{MA}(t) \leftarrow \frac{1}{A} \sum_{n=t}^{t+A} Err_{GS}(n)$ ▷ A-sample-wide moving average of $Err_{GS}(t)$
    $t_{reset} \leftarrow \{t | Err_{GS}^{MA}(t) > \mu\}$ ▷ Indentify t violating the error threshold
    $\hat{s}(t_{reset}) \leftarrow \hat{s}(t_{reset}) \exp j\angle rand(t_{reset})$ ▷ Phase reset
  end if
end for
return $\hat{s}(t)$

accumulated error. However, under the post-equalization scheme, the signals entering the GS algorithm are still distorted and need to be continuously equalized during the algorithm iterations, which leads to an increase in the algorithm accumulated error. On the other hand, whether it is pre-equalization or post-equalization, the diminished OSNR penalty observed in schemes $S1$ and $S3$, which rely on the GS-aided estimation method, is more pronounced compared to schemes $S2$ and $S4$, which are based on the data-aided estimation method. In addition, $S1$ and $S2$ based on the LMS algorithm are better than $S3$ and $S4$ based on the LS algorithm.

Additionally, we conducted an investigation into the influence of diverse E/O frequency response bandwidth limitations on the performance of pre-equalization and post-equalization based on the four estimation schemes, all under an OSNR of 28 dB. Fig. 9 shows the BERs versus frequency response bandwidth limitations to achieve a 7% FEC threshold. As we can see, two compensation schemes significantly reduce the E/O bandwidth penalty, thereby mitigating the dependence of carrierless PR receivers on the E/O bandwidth limitation. In the case of pre-equalization schemes based on $S1$, $S2$, $S3$, and $S4$, respectively, the bandwidth sensitivity is improved by 0.76, 0.36, 0.54, and 0.34 GHz. In the corresponding post-equalization case, the bandwidth penalty is reduced by 0.44, 0.26, 0.38, and 0.22 GHz,

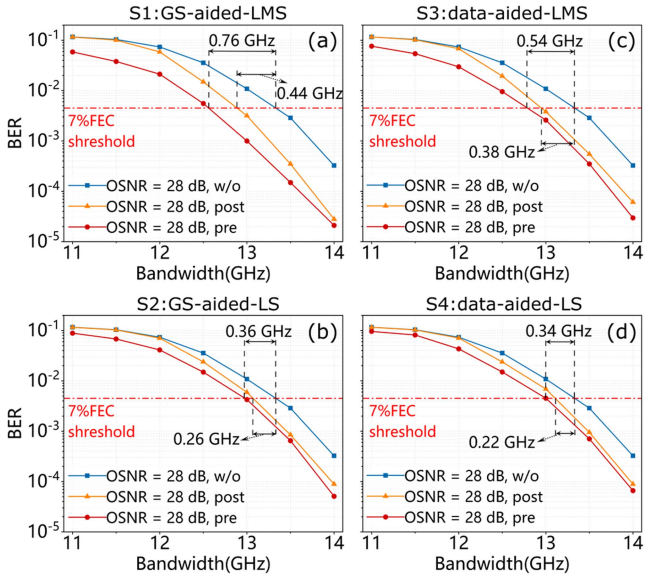

Fig. 9. Simulated BERs versus frequency response bandwidth limitations under (a) $S1$, (b) $S2$, (c) $S3$, (d) $S4$ schemes.

respectively. Indeed, even when the E/O bandwidth is low, pre-equalization demonstrates superior robustness compared to post-equalization, owing to its independence from link noise during the pre-equalization process. Besides, LMS-based algorithm perform more E/O bandwidth sensitivity than LS-based algorithm. GS-aieded schemes have reduced penalties compared with their date-aided counterparts. To sum up, simulation results of the performance of the pre-equalization and post-equalization reveal the dependence of carrierless PR receivers on OSNR and E/O bandwidth limitations can be effectively reduced by employing the proposed compensation schemes.

IV. Experiments

A. Experimental Setup

In this section, we experimentally validate the performance of the proposed E/O frequency response estimation and compensation schemes. The experimental setup for detecting a single-polarization carrierless 30-GBaud QPSK signal using the PR receiver is shown in Fig. 10. In the experiment, an external cavity laser with a linewidth of 100 kHz at 1550.06 nm was modulated by an in-phase and quadrature Mach—Zehnder modulator (IQ-MZM). The digital-to-analog converter (DAC) operating at 60 GSamples/s generated a Nyquist-shaped 30-GBaud QPSK signal (roll-off $\beta = 0.01$) with a length of 2^{17} samples. For Scheme 1: pre-equalization, an FIR pre-equalizer is applied to the data loaded into the Digital to Analog Converter (DAC) to compensate for the distortion from the E/O frequency response, consistent with the process in Section II-C. A span of 55-km SMF was used for transmission, providing 885.5 ps/nm accumulated dispersion at the Rx. Two EDFAs are set at both ends of the 55-km fiber span. We use the optical filter with a 3-dB bandwidth of 1.2 nm to filt out out-of-band noise. Within the PR receiver, the optical field was split into two by an asymmetric optical

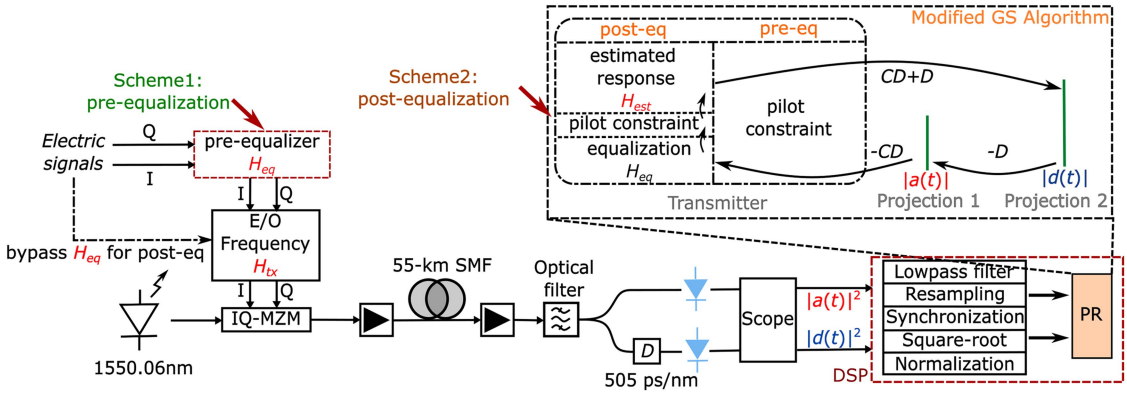

Fig. 10. Experimental setup for transmission over 55-km SMF including pre-equalization and post-equalization.

splitter to compensate for the insertion losses of the dispersive element with 505 ps/nm, used for alternative projection. The optical power entering the dispersive element is approximately 4 dBm. After direct detection, both optical intensity signals are sampled by a digital sampling oscilloscope and undergo digital resampling to two SPS as $|a(t)|^2$ and $|d(t)|^2$. Due to practical limitations in the bandwidth of the PDs, frequency response compensation is conducted on the two intensity signals [18]. After digital signal prepossessing, two amplitude waveforms of $s(t)$, namely, $a(t)$ and $d(t)$ are generated and sent to the modified GS algorithm. The experimental system uses a 20% pilot symbol ratio and the Rx employs the pilot symbol constraint. CD and $-CD$ stand for the dispersion coefficient of fiber channel forward and backward propagation, respectively. For Scheme 2: post-equalization, the modified GS algorithm is combined with the estimation impulse response and the equalization response, consistent with the pseudocode in Section III-A.

B. Experimental Results

Before validating the performance of the two compensation schemes, we initially estimate the E/O frequency response bandwidth in the experiment. A training sequence consisting of 2048 training QPSK symbols is transmitted. The OSNR at the Tx measured by a spectrometer is 30 dB. The ROP of two intensity signals is measured after two PDs and set at 3 dBm. In order to suppress the distortion caused by the O/E frequency response of the Rx, we estimate and equalize the frequency response of the two PDs at the Rx, which is also our main work in [18]. Estimated E/O normalized power frequency response is shown in Fig. 11(a). The measured optical spectra at Tx is given in Fig. 11(b). It can be find that the estimated amplitude-frequency response envelope tends to be consistent with that of the spectrum. Fig. 11(c) and (d) present the estimated normalized power phase frequency response under four estiamtion schemes. The flatness of both the spectrum and phase profiles within the signal bandwidth suggests that the dispersive element introduces only negligible distortion.

Fig. 12 shows the measured BER versus ROP for pre-equalization and post-equalization under (a) $S1$, (b) $S2$, (c) $S3$, (d) $S4$ in the experiment. We adjust the pump power of EDFA at

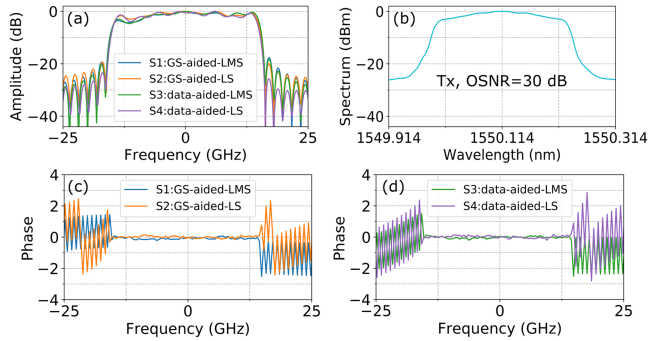

Fig. 11. (a) Estimated E/O normalized power frequency response. (b) Measured optical spectra. Estimated normalized power phase frequency response under (c) $S1$, $S2$ and (d) $S3$, $S4$.

the Rx to obtain different ROPs. It can be seen that to reach the 20% FEC threshold (BER $= 2.2 \times 10^{-2}$), both pre-equalization and post-equalization have reduced the dependence on the ROP comparing to without any compensation schemes. In the case of pre-equalization based on the $S1$, $S2$, $S3$, and $S4$, respectively, the ROP sensitivity has increased by 0.69 dB, 0.34 dB, 0.51 dB, and 0.42 dB. In the corresponding post-equalization case, the ROP sensitivity has increased by 0.42 dB, 0.17 dB, 0.32 dB, and 0.07 dB, respectively. In low ROP scenarios, the performance improvement of pre-equalization is more noticeable than that of post-equalization, further confirming the robustness of pre-equalization. The GS-aided estimation algorithm exhibits a clear performance advantage over the data-aided algorithm, especially in scenarios with higher ROP, such as 3 dBm ROP. Moreover, the LMS-based algorithm outperforms the LS-based algorithm, confirming that the LMS algorithm is better suited for channel estimation.

Fig. 13 shows the measured BER versus the number of iterations for (a) pre-equalization and (b) post-equalization based on four estimation schemes at 30 dB OSNR. In comparison to the absence of any compensation scheme, both pre-equalization and post-equalization lead to a reduction in BER of PR receiver demodulation. For both compensation schemes, $S1$ based on the GS-aided estimation method and the LMS channel estimation algorithm demonstrates the most significant

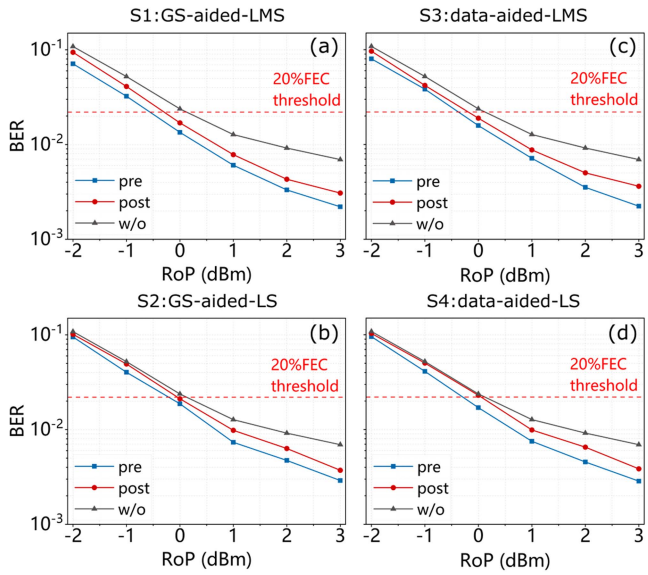

Fig. 12. Measured BER versus ROP for pre-equalization and post-equalization under (a) $S1$, (b) $S2$, (c) $S3$, (d) $S4$.

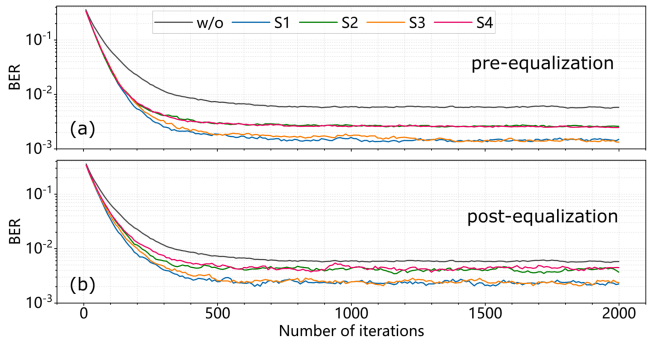

Fig. 13. Measured BER versus the number of iterations for (a) pre-equalization and (b) post-equalization based on four estimation schemes at ROP values of 3 dBm.

performance improvement among the four estimation schemes. In the case of pre-equalization and post-equalization, $S1$ reduce the BER after full convergence from 6.9×10^{-3} to 2.2×10^{-3} and 3.1×10^{-3}, respectively. To reach 7% FEC threshold level, $S1$ has a fastest convergence speed and take only 230 and 270 iterations under pre-equalization and post-equalization, respectively. $S3$ shows a similar performance to $S1$ after convergence while $S2$ and $S4$ based on the LS algorithm show slightly inferior performance. Furthermore, it is worth to note that pre-equalization shows more desirable performance improvement. Fig. 14 shows the constellations for the demodulated QPSK signal (a) without compensation, with (b) pre-equalization and (c) post-equalization at ROP values of 3 dBm. The compensation outcomes achieved through estimation scheme S1 are the most favorable, indicating the superior performance of the GS-aided estimation method compared to the data-aided estimation method, as well as the superiority of the LMS-based channel estimation algorithm over the LS-based channel estimation algorithm. Moreover, regardless of the estimation scheme

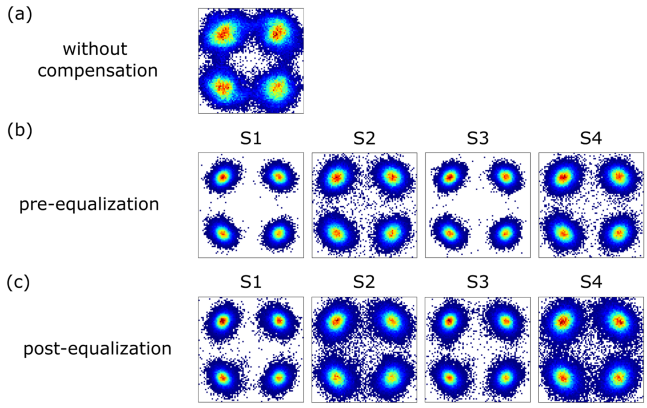

Fig. 14. Constellation for the demodulated QPSK signal (a) without compensation, with (b) pre-equalization and (c) post-equalization at ROP values of 3 dBm.

used, pre-equalization demonstrates higher robustness under conditions of low OSNR and low E/O bandwidth limitations.

V. Conclusion

In this study, two estimation methods named GS-aided and data-aided are proposed in order to know the complex-valued E/O channel response in the absence of phase information. Two channel estimation algorithms including LMS and LS are combined with the proposed GS-aided and data-aided methods respectively to form four estimation schemes. Furthermore, two compensation schemes named pre-equalization and post-equalization perform at the transmitter side and the Rx respectively are implemented and compared by simulations and experiments. Simulation results validate the improved OSNR and bandwidth sensitivity using proposed methods. We and experimentally transmit a training sequence consisting of training QPSK symbols to estimate the E/O conversion frequency response under four estimation schemes, results show all schemes successfully estimate the frequency response in the absence of phase information. To verify the performance of the compensation schemes, a single-polarization carrierless 30-GBaud QPSK signal is experimentally detected and recovered using the PR carrier employing proposed pre-equalization and post-equalization. The experimental results demonstrate that pre-equalization exhibits greater robustness compared to post-equalization. Pre-equalization based on GS-aided-LMS method reduce the BER from 6.9×10^{-3} to 2.2×10^{-3} after full convergence at ROP values of 3 dBm. Our research demonstrates that the performance of PR receivers have potential to be further improved once they know information about channel impairments induced by the transmitter, regardless of measuring the phase. As no signal-carrier beating is required in the detection process, carrierless PR receivers could be an attractive solution to be employed in short-reach applications such data-center interconnects in the future. The next phase of our work is to conduct real-time performance testing of the proposed estimation and equalization scheme to further explore its robustness in a real-time signal processing environment.

REFERENCES

[1] X. Zhou, H. Liu, R. Urata, and S. Zebian, "Scaling large data center interconnects: Challenges and solutions," *Opt. Fiber Technol.*, vol. 44, pp. 61–68, 2018. [Online]. Available: https://www.sciencedirect.com/science/article/pii/S1068520017302432

[2] S. Derrible and C. Kennedy, "The complexity and robustness of metro networks," *Physica A: Stat. Mechanics Appl.*, vol. 389, no. 17, pp. 3678–3691, 2010. [Online]. Available: https://www.sciencedirect.com/science/article/pii/S0378437110003262

[3] S. H. Kim, H. S. Chung, and S. M. Kim, "Experimental demonstration of CPRI data compression based on partial bit sampling for mobile front-haul link in C-RAN," in *Proc. Opt. Fiber Commun. Conf.*, 2016, Paper W1H-5. [Online]. Available: https://opg.optica.org/abstract.cfm?URI=OFC-2016-W1H.5

[4] B. Glance, "Polarization independent coherent optical receiver," *J. Lightw. Technol.*, vol. 5, no. 2, pp. 274–276, Feb. 1987. [Online]. Available: https://ieeexplore.ieee.org/abstract/document/1075494/authors#authors

[5] D.-Z. Hsu, C.-C. Wei, H.-Y. Chen, W.-Y. Li, and J. Chen, "Cost-effective 33-Gbps intensity modulation direct detection multi-band OFDM LR-PON system employing a 10-GHz-based transceiver," *Opt. Exp.*, vol. 19, no. 18, pp. 17546–17556, Aug. 2011. [Online]. Available: https://opg.optica.org/oe/abstract.cfm?URI=oe-19-18-17546

[6] A. Mecozzi, C. Antonelli, and M. Shtaif, "Kramers–Kronig coherent receiver," *Optica*, vol. 3, no. 11, pp. 1220–1227, Nov. 2016. [Online]. Available: https://opg.optica.org/optica/abstract.cfm?URI=optica-3-11-1220

[7] H. Ji et al., "High-dimensional stokes vector direct detection over few-mode fibers," *Opt. Lett.*, vol. 44, no. 8, pp. 2065–2068, Apr. 2019. [Online]. Available: https://opg.optica.org/ol/abstract.cfm?URI=ol-44-8-2065

[8] M. Matsumoto, "Phase reconstruction scheme using dispersive media in direct detection," in *Proc. IEEE Opt. Fiber Commun. Conf. Exhib.*, 2020, pp. 1–3.

[9] T. Quatieri and A. Oppenheim, "Iterative techniques for minimum phase signal reconstruction from phase or magnitude," *IEEE Trans. Acoust., Speech, Signal Process.*, vol. 29, no. 6, pp. 1187–1193, Dec. 1981.

[10] C. Sun, D. Che, H. Ji, and W. Shieh, "Towards low carrier-to-signal power ratio for Kramers-Kronig receiver," in *Proc. IEEE Opt. Fiber Commun. Conf. Exhib.*, 2019, pp. 1–3.

[11] L. Blech, C. Antonelli, A. Mecozzi, Y. C. Eldar, and M. Shtaif, "Enhancing the Kramers–Kronig receiver via dispersion-based spatial diversity," *Opt. Lett.*, vol. 45, no. 13, pp. 3494–3497, Jul. 2020. [Online]. Available: https://opg.optica.org/ol/abstract.cfm?URI=ol-45-13-3494

[12] S. An, Q. Zhu, J. Li, and Y. Su, "Accurate field reconstruction at low CSPR condition based on a modified KK receiver with direct detection," *J. Lightw. Technol.*, vol. 38, no. 2, pp. 485–491, Jan. 2020.

[13] H. Chen, N. K. Fontaine, J. M. Gene, R. Ryf, D. T. Neilson, and G. Raybon, "Dual polarization full-field signal waveform reconstruction using intensity only measurements for coherent communications," *J. Lightw. Technol.*, vol. 38, no. 9, pp. 2587–2597, May 2020. [Online]. Available: https://opg.optica.org/jlt/abstract.cfm?URI=jlt-38-9-2587

[14] H. Chen et al., "Mode-multiplexed full-field reconstruction using direct and phase retrieval detection," in *Proc. Opt. Fiber Commun. Conf.*, 2020, Paper W4A-5. [Online]. Available: https://opg.optica.org/abstract.cfm?URI=OFC-2020-W4A.5

[15] Y. Yoshida, T. Umezawa, A. Kanno, and N. Yamamoto, "A phase-retrieving coherent receiver based on two-dimensional photodetector array," *J. Lightw. Technol.*, vol. 38, no. 1, pp. 90–100, Jan. 2020. [Online]. Available: https://opg.optica.org/jlt/abstract.cfm?URI=jlt-38-1-90

[16] H. Chen, H. Huang, N. K. Fontaine, and R. Ryf, "Phase retrieval with fast convergence employing parallel alternative projections and phase reset for coherent communications," *Opt. Lett.*, vol. 45, no. 5, pp. 1188–1191, Mar. 2020. [Online]. Available: https://opg.optica.org/ol/abstract.cfm?URI=ol-45-5-1188

[17] H. Huang et al., "Distortion-aware phase retrieval receiver for carrierless high-order QAM transmission," *J. Lightw. Technol.*, early access, Jan. 5, 2024, doi: 10.1109/JLT.2024.3350090.

[18] Q. Gao, H. Huang, H. Chen, N. K. Fontaine, R. Ryf, and Y. Song, "Effect of O/E front-end frequency response on carrier-less phase retrieval receiver and its compensation," in *Proc. CLEO: Appl. Technol. Conf.*, 2023, Paper JTh2A-140. [Online]. Available: https://opg.optica.org/abstract.cfm?URI=CLEO_SI-2023-JTh2A.140

[19] B. Widrow, J. McCool, and M. Ball, "The complex LMS algorithm," *Proc. IEEE*, vol. 63, no. 4, pp. 719–720, Apr. 1975.

[20] Y. Qiao, S. Yu, P. Su, and L. Zhang, "Research on an iterative algorithm of LS channel estimation in MIMO OFDM systems," *IEEE Trans. Broadcast.*, vol. 51, no. 1, pp. 149–153, Mar. 2005.

[21] Z. Tang, R. C. Cannizzaro, G. Leus, and P. Banelli, "Pilot-assisted time-varying channel estimation for OFDM systems," *IEEE Trans. Signal Process.*, vol. 55, no. 5, pp. 2226–2238, May 2007.

[22] Y. Neuvo, D. Cheng-Yu, and S. Mitra, "Interpolated finite impulse response filters," *IEEE Trans. Acoust., Speech, Signal Process.*, vol. 32, no. 3, pp. 563–570, Jun. 1984.